ACS OMEGA

Open Access

http://pubs.acs.org/journal/acsodf

Article

Synergistic Role of the AuAg-Fe_3O_4 Nanoenzyme for Ultrasensitive Immunoassay of Dengue Virus

Uddipan Dasgupta, Malabika Ghosh, Rupali Gangopadhyay, Nguyen Thi Ngoc Anh, Ruey-An Doong, Provash Chandra Sadhukhan, and Ankan Dutta Chowdhury*

Cite This: *ACS Omega* 2024, 9, 40051−40060

Read Online

ACCESS | Metrics & More | Article Recommendations | Supporting Information

ABSTRACT: A combination of magnetic and noble metal nanoparticles (NPs) has recently emerged as a potential substance for rapid and sensitive immunosorbent assays. However, to make the assay an alternative method for Enzyme-linked immunosorbent assay, the individual role of each nanoparticle must be explored properly. In this work, an immunoassay has been proposed using two antibody-conjugated iron oxide nanoparticles (Fe_3O_4NPs) and gold−silver bimetallic nanoparticles (AuAgNPs) to enhance the sensitivity of virus detection by colorimetric TMB/H_2O_2 signal amplification. A synergistic effect is monitored between Fe_3O_4NPs and AuAgNPs, which is explored for colorimetric virus detection. The sensor exploits the synergistic effect between the nanoparticles to successfully detect a wide range of dengue virus-like particle (DENV-LP) concentrations ranging from 10 to 100 pg/mL with a detection limit of up to 2.6 fg/mL. In the presence of a target DENV-LP, a sandwich-like structure is formed, which restricts the electron transfer and the associated synergistic effect between the nanoparticles, restricting the TMB oxidation process. Therefore, the synergistic effect is the key to the present work, which accounts for the enhanced rate of the enzymatic reaction on TMB and makes the current method of virus detection more sensitive and reliable compared to the others.

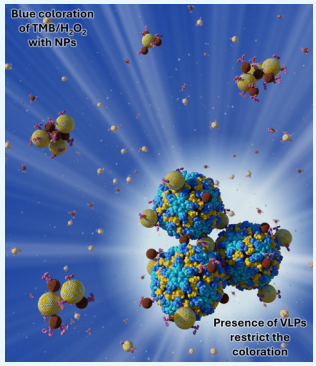

INTRODUCTION

The detection of viruses holds immense importance in various domains, from healthcare to biotechnology, with far-reaching implications for public health and research.[1−3] Rapid and accurate virus detection plays a pivotal role in curbing outbreaks, understanding disease dynamics, and developing effective interventions.[1,4−9] Thus, the development of advanced virus detection methods that offer enhanced sensitivity, speed, and reliability is necessary to combat these challenges effectively.[10−13] Enzyme-linked immunosorbent assay (ELISA) has long been a foundation in virus detection due to its specificity and simplicity.[14−16] However, this technique is complex and time-consuming and also involves multiple incubation and washing steps, which are few major drawbacks, which might limit rapid, high-throughput screening.[7,12,17] It relies on specialized laboratory equipment like microplate readers for precise measurements, limiting its application in resource-limited settings.[14,18] Nonspecific binding in ELISA can further reduce its accuracy and reliability, while variations between assay runs and personnel conducting the tests can affect the reproducibility of results.[18]

Considering the drawbacks associated with ELISA, there are several attempts made to find alternative NP-based methods with rapid methodologies.[19] Noble metal NPs possess inherent enzyme-like capabilities, exceptional stability, customizable optical characteristics, and versatile surface chemistry. These unique properties of NPs enable faster and more sensitive detection, making them a promising alternative for developing rapid, robust, and high-throughput immunoassay platforms.[20−22] Recently, several research groups have developed nanoparticle-based immunoassays for signal amplification where a few reports have incorporated magnetic nanoparticles as better separating particles.[23−26] Earlier, Xianyu et al. have introduced a novel plasmonic immunoassay using a horseradish peroxidase (HRP) and iodide-mediated cascade reaction to enhance gold nanoparticle aggregation, which offered high sensitivity and visual readout.[27] Lu et al. have introduced a modified immunoassay method using enzyme-catalyzed silver shell deposition on gold nanorods to achieve high sensitivity for prostate antigen detection.[28] The nanoparticle has been modified by Khoris et al., who have developed a colorimetric bioassay for norovirus detection using gold−silver nanohybrid NPs with enhanced peroxidase activity and vivid color change.[29] While these groups have introduced notable immunoassay signal amplification methods, there are inherent concerns regarding the specificity due to potential interference from other substances binding to nanoparticles. To overcome this issue, innovative approaches have been made using magnetic NPs that offer unique

Received: June 26, 2024
Revised: August 27, 2024
Accepted: August 29, 2024
Published: September 10, 2024

advantages in enhancing biosensor precision and sensitivity. For example, iron oxide NPs have been included in the system for their ability to facilitate magnetic separation, providing a significant advantage in isolating viral targets, even in trace amounts.[24,30−32] Ross et al. have effectively isolated soluble transferrin receptors following magnetic separation using Fe_3O_4NPs functionalized with antibodies (Ab); this technique eventually enhanced the precision and reliability of the biosensor.[33] Fe_3O_4NP, on the other hand, exhibits slow but steady intrinsic enzyme-like activity akin to horseradish peroxidase (HRP).[34] For example, Oh et al. utilized Fe_3O_4NPs and AuNPs to detect the influenza A virus. The AuNPs were used for their peroxidase-like activity, and magnetic Fe_3O_4NPs coated with silicon dioxide were used to enable specific magnetic separation of the analyte after elimination of their own peroxidase activity.[24]

Individually, iron oxide is not a considerable substrate for colorimetric processes; however, it shows a significant effect when combined with a metal nanoparticle for TMB oxidation, which is explored in this study. We have investigated significant enhancement of the TMB oxidation process by the controlled inclusion of iron oxide nanoparticles. In addition, their combined structure has been theoretically simulated to understand the smooth electron transfer process by the energy-minimized structure, resulting in a synergistic effect. The potential role of iron oxide nanoparticles, especially when combined with other noble metal nanoparticles, in the TMB coloration process had not been explored until now. All earlier methods either ignored or mask the iron oxide layer with a protective polymer layer, as discussed elsewhere.

In the present work, an immunoassay has been developed by combining antibody-conjugated iron oxide nanoparticles (Fe_3O_4NPs) and antibody-conjugated gold−silver bimetallic nanoparticles (AuAgNPs) to enhance the sensitivity of detection of DENV-LP, selected as an antigen to establish the underlying mechanism. The bimetallic nanoparticles show superior TMB oxidation (coloration) compared to bare silver (AgNPs) or AuNPs.[29] It was observed that the coloration of the TMB shows higher intensity in the presence of both Fe_3O_4NP and AuAgNP in close association, compared to pure AuAgNPs; this might be the result of the synergistic effect between these two nanoparticles, as depicted in the schematic diagram in Figure 1. When the virus particles are selectively captured by antibody-conjugated Fe_3O_4NPs and AuAgNPs, a sandwich formation takes place, which restricts the electron transfer and the resulting synergistic effect between the two NPs. Therefore, the synergistic integration in this work, exploiting Fe_3O_4NP-based target isolation and AuAgNP-catalyzed signal amplification, represents a significant step forward in virus detection, greatly enhancing both sensitivity and selectivity.

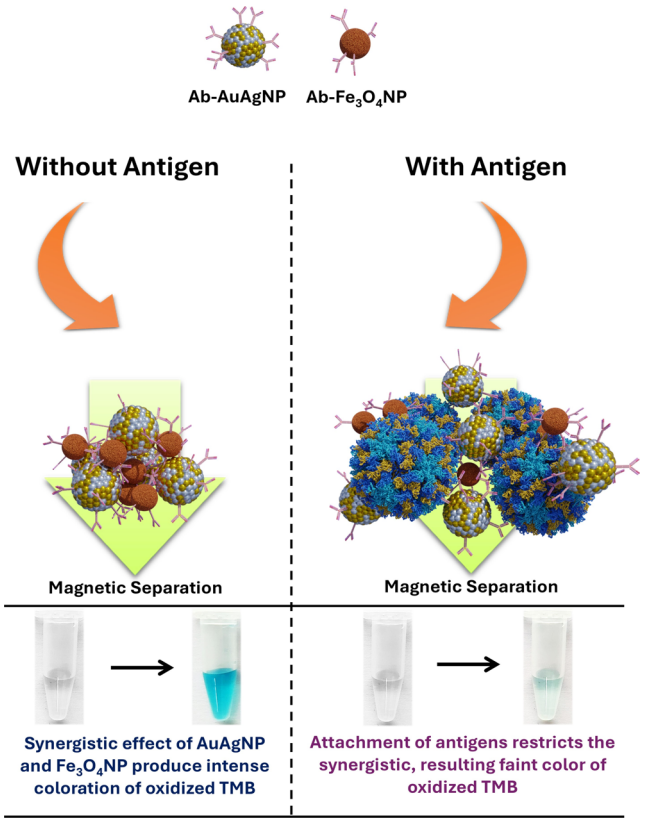

Figure 1. Schematic representation of the AuAgNP and Fe_3O_4NP interaction with TMB/H_2O_2 in the presence of the target DENV-LP.

MATERIALS AND METHODS

Chemicals. Iron(II) chloride and iron(III) chloride were purchased from Loba Chemie; 25% NH_4OH (ammonium hydroxide) and toluene were obtained from Merck. APTES (3-aminopropyltriethoxysilane) and EDC (1-ethyl-3-(3-(dimethylamino)propyl) carbodiimide) were procured from Sigma-Aldrich. NHS (*N*-hydroxysuccinimide) was sourced from TCI. Methanol, silver nitrate, DMSO (dimethyl sulfoxide), hydrogen peroxide, and sulfuric acid were also supplied by Merck. Dengue antibody (1 mg/mL) was purchased from GeneTex. Gold chloride and sodium citrate were obtained from Thermo Scientific. TMB (3,3′,5,5′-tetramethylbenzidine) was acquired from Sigma-Aldrich. DENV-LP was provided by Enoch Y. Park from Shizuoka University, Japan. All chemicals were used without further purification, and double-distilled water was used throughout the experiment.

Synthesis and Antibody Conjugation of Iron Oxide Nanoparticles. The iron oxide nanoparticle synthesis and APTES modification were adapted from the previous work.[35,36] Iron(II) chloride (0.5 g) and iron(III) chloride (1.35 g) were mixed in 50 mL of water in a beaker at room temperature for 1 h. The mixture was then transferred to a two-neck flask, sealed with corks, and heated to 60 °C while stirring in a water bath for 30 min, turning the solution brown. Subsequently, 33 mL of 25% NH_4OH was rapidly added, causing the solution to turn black, and it was stirred for an additional 2 h. Magnetic separation was then performed, washing with water three times. The obtained pellet was oven-dried overnight at 70 °C, scraped, and ground into 0.6 g of powder using a mortar and pestle. This powder was sonicated in a mixture of 40 mL of toluene and 20 mL of methanol for 15 min and heated to 70 °C to evaporate the solvents. Next, 1 mL of APTES was added and stirred for 2 h while keeping the flask in a water bath at 70 °C. The nanoparticles were magnetically separated, washed with toluene three times, and then air-dried. For antibody conjugation, 20 μL of dengue antibody (1 μg/mL) was incubated with 20 μL of 200 mM EDC for 10 min, followed by addition of 20 μL of 100 mM NHS for 15 min. Finally, these activated antibodies were added to 200 μL of 2.5 mg/mL APTES-coated iron oxide nanoparticles in water.

https://doi.org/10.1021/acsomega.4c05937
ACS Omega 2024, 9, 40051−40060

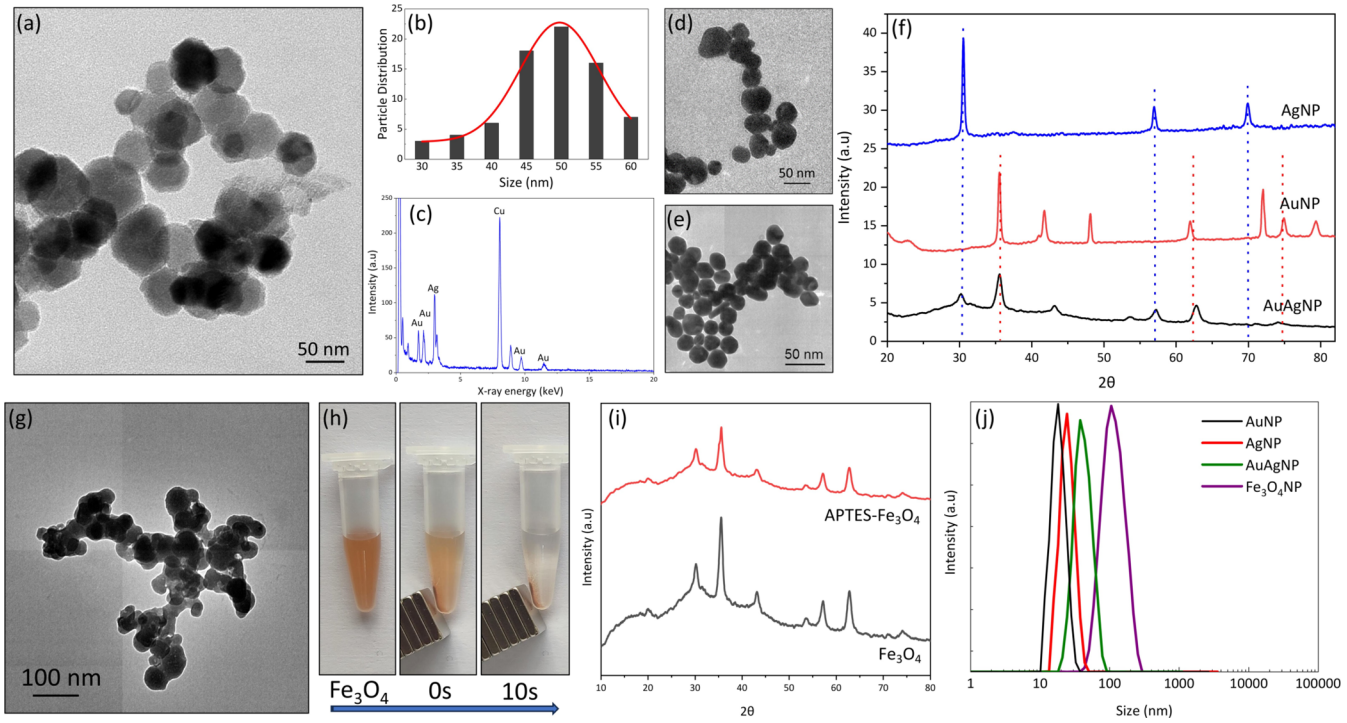

Figure 2. Characterization of nanoparticles: (a) TEM image of AuAgNPs, (b) size distribution of AuAgNPs, (c) EDX data of AuAgNPs, (d) TEM image of bare AgNPs, (e) TEM image of bare AuNPs, (f) XRD of AgNPs, AuNPs, and AuAgNPs, (g) TEM image of Fe_3O_4NPs, (h) images of the magnetic property of Fe_3O_4NPs, (i) XRD of Fe_3O_4NPs before and after APTES coating, and (j) DLS spectra of AuNPs, AgNPs, AuAgNPs, and Fe_3O_4NPs.

Synthesis and Antibody Conjugation of Gold−Silver Bimetallic Nanoparticles. Gold−silver bimetallic nanoparticles were synthesized based on the method by Blommaerts et al.[37] with slight modifications. In a conical flask, 800 μL of 0.01 M silver nitrate was mixed with 98 mL of water while stirring. The solution was heated until just before boiling, and then, 200 μL of 0.01 M gold chloride was added. After the mixture was boiled, 1 mL of 1% sodium citrate was added. Within 10 min, a yellow solution formed, which stabilized after 15 min of continued heating. The mixture was heated until concentrated to 1.5 mL, then cooled, centrifuged at 10 000 rpm for 20 min to yield a 150 μL pellet, and washed twice with water. To this pellet, 25 μL of dengue antibody (1 μg/mL) was added, mixed, and incubated overnight at 4 °C. Bare AgNPs and AuNPs were also synthesized for comparative studies, following the standard route of synthesis.[29,38]

TMB Solution Preparation. A TMB solution optimized for the assay was made by dissolving TMB at 2.5 mg/mL in DMSO. For the assay, 100 μL of TMB solution was freshly mixed with 900 μL of a pH 4 citrate phosphate buffer and 50 μL of 33% hydrogen peroxide.

Assay for DENV-LP Detection. For the assay, 2 μL of antibody-conjugated Fe_3O_4NPs were incubated with 10 μL of antigen sample for 10 min at room temperature. Subsequently, 2 μL of antibody-conjugated AuAgNPs was added and further incubated for around 30 min at room temperature to allow sandwich complex formation. Magnetic separation was then performed by vigorously shaking the sample tube and immediately placing it over a magnet for 10 s to isolate the nanoparticle−antigen−antibody complex pellet. The supernatant was discarded, and the pellet was resuspended thoroughly in 200 μL of TMB substrate solution. This was incubated for 3 min at room temperature to allow color development. The enzymatic reaction was stopped by the addition of 10 μL of 0.5 M sulfuric acid, and absorbance was measured by absorbance spectroscopy to quantify the antigen. For the negative control, phosphate buffer at pH 7 was added instead of the antigen sample, while keeping all other assay conditions the same.

Characterizations. Transmission electron microscopy (TEM) images were obtained using a JEOL JEM-2010 instrument at an accelerating voltage of 200 kV. The crystalline phases of the samples were characterized by X-ray diffraction (XRD) using a Bruker D8 X-ray diffractometer with Ni-filtered Cu Kα radiation (λ = 1.5406 Å). The hydrodynamic diameter and zeta potential of the nanoparticles were determined by dynamic light scattering (DLS) measurements using a Zetasizer Nano ZS instrument from Malvern, UK. Absorbance spectra of the samples dispersed in the buffer were recorded using a Hitachi U-2900 spectrophotometer with a slit width of 1.5 nm and a scanning speed of 1200 nm/min.

Theoretical modeling was conducted to understand the uniqueness of the system. This involved analyzing the energy-minimized structures of TMB, AuAgNP, and AuAg-Fe_3O_4NP. These structures were built using Chemcraft before conducting modeling studies with density functional theory (DFT) as implemented in the Gaussian 03 suite of programs.[39] The structures were determined by full geometry optimization in the gas phase using the B3LYP functional[39] with a moderate basis set (3-21G/6-31G**/LANL2DZ) for a balance between accuracy and computational resources. Due to computational limitations, an arbitrarily chosen nanocluster Ag_6Au_2NP was formed and optimized using the LANL2DZ basis set. This nanocluster was then combined with Fe_3O_4 and partially optimized again using the same basis set. The structural data of the Fe_3O_4 nanocluster were initially obtained from the

https://doi.org/10.1021/acsomega.4c05937
ACS Omega 2024, 9, 40051−40060

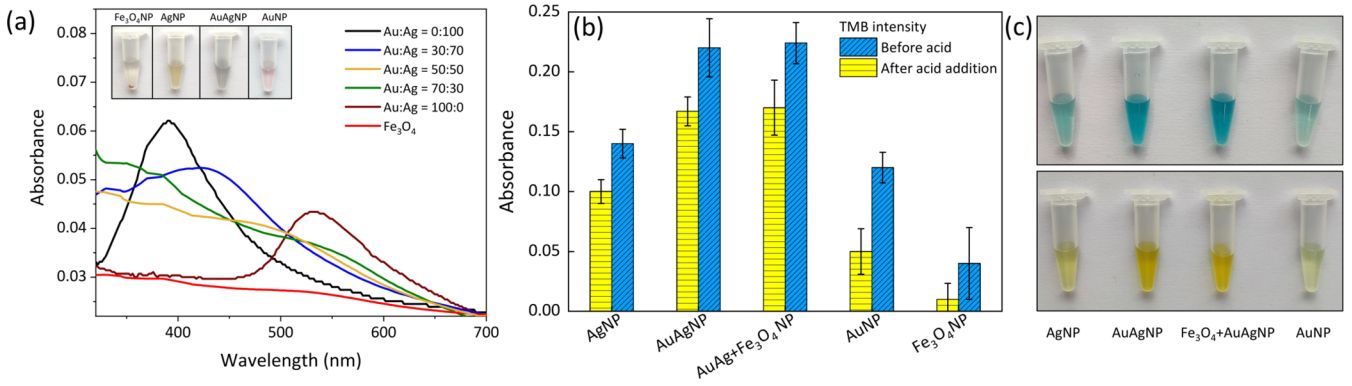

Figure 3. Catalytic properties of nanoparticles: (a) absorbance spectra of various ratios of Au and AgNPs and Fe_3O_4NPs (b) TMB color intensity with various NPs, before and after the addition of stop solution (c) visual coloration of TMB/H_2O_2 in the presence of different nanomaterials (blue means oxidized TMB color and yellow means after addition of the stop solution, 0.5 M H_2SO_4).

Mercury database and optimized during the work. Results of structural optimization of TMB, alloy nanoclusters, and their combination are discussed in the relevant sections. The charge distribution for all systems was determined using Mulliken's method. The frontier molecular orbitals, especially the highest occupied molecular orbital (HOMO) and the lowest unoccupied molecular orbital (LUMO) of AuAg-Fe_3O_4NP, were analyzed. The structures of the molecular orbitals (MOs) and electronic charge densities were visualized by using Chemcraft.

RESULTS AND DISCUSSION

This work presents a technique for colorimetric detection of DENV-LP by TMB oxidation using AuAgNPs and Fe_3O_4NPs. The concept of sensing is based on the sandwich formation between two nanocomposites in the presence of DENV-LP, as depicted in Figure 1. To prepare the detection probe, antibodies were immobilized on the nanoparticles via EDC/NHS covalent chemistry.[40,41]

Both AuAgNPs and Fe_3O_4NPs are capable of oxidizing TMB individually; however, their mode of action and rate of interaction are different. AuAgNPs can oxidize TMB in a rapid process and takes 200 s to reach saturation, while the Fe_3O_4NP takes at least 10 min to initiate the reaction (Figure S1). AuAgNPs show enhanced peroxidase-like activity as a nanozyme compared with bare AuNPs and AgNPs.[29,42] Silver deposition on the gold surface increased the affinity of the nanohybrid for H_2O_2 and simultaneously enhanced the reaction with TMB due to the increase in more available reactive species. However, the mixture of these AuAgNPs and Fe_3O_4NPs show a higher rate of oxidation in the same reaction conditions (within 180 s), confirming the synergistic effect between Fe_3O_4NPs and AuAgNPs. Due to the large size of AuAgNPs, they are coprecipitated with Fe_3O_4NPs and remain closely connected in the absence of DENV-LP. After the addition of TMB, the synergistic effect of the AuAgNPs and Fe_3O_4NPs contribute to the oxidation process and forms the intense blue coloration as depicted in Figure 1. In the presence of DENV-LP, a sandwich-like structure is formed between two nanoparticles. It is anticipated that the presence of a virus between two nanoparticles restricts the connectivity between the two nanoparticles, eventually prohibiting the synergistic effect. As a result, the coloration of the sensor shows an inverse proportion with increasing concentration of the virus. Hence, the AuAgNP−Fe_3O_4NP combination exhibits an enzymatic role in the oxidation process of TMB and serves as a capture probe to recognize the target DENV-LP.

Characterization of Nanoprobes. TEM images of AuAgNPs show the spherical shape of the alloy NPs with an average size of 50 ± 1.0 nm (Figure 2(b)), which is bigger compared to bare AgNPs (15 nm) and AuNPs (12 nm), presented in Figure 2(d,e). In the TEM image (Figure 2(a)), distinct dense and light shades are observable, confirming the formation of an alloy of AuAgNPs. Different locations of the TEM grids are also analyzed for EDAX analysis to find the molecular composition of the AuAgNP. It can be shown in Figure 2(c) that the prominent peaks of Au and Ag are presented along with a sharp peak of Cu (from the copper grid), confirming the successful synthesis of the combined NPs. Crystal structural data of AuAgNPs are deciphered by using XRD along with its counterparts AuNPs and AgNPs (Figure 2(f)). The diffraction patterns of (111) were obtained at approximately 37° for both AuNPs and AuAgNPs. Two more sharp peaks at 63 and 75° of AuNPs are also observed for AuAgNPs, confirming the presence of Au in the lattice of the AuAgNPs. Similarly, the characteristic peaks of AgNPs at 30, 58, and 70° are also noticeable in AuAgNPs, although few peaks in AuAgNPs become flatter compared to bare Au and AgNPs due to the masking effect of various crystal planes. However, the presence of crystal planes from both nanoparticles confirms the structure of the AuAgNP as a bimetallic crystal.

In the TEM images, the Fe_3O_4NPs show a spherical shape with an average size of 60 nm (Figure 2(g)). Due to its magnetic properties, some coagulation has been observed; however, the size variation is almost negligible. The magnetic particles were easily separated using an external magnet in 10 s, as shown in Figure 2(h). Its crystalline properties are shown in Figure 2(i), exhibiting its characteristic peaks at 2θ at 30, 37, and 57°.[43,44] After silanization with APTES, there is no change in the XRD pattern, whereas the surface charge in zeta potential changes from −35.3 to +29.9 mV due to amine group insertion (Figure S2).[45] The coating of the APTES is also confirmed by the FTIR spectroscopy, where the insertion of amine groups by replacing the hydroxyl groups on the surface of Fe_3O_4NPs has been noticed (Figure S3). These observations confirm the successful coating of APTES on the surface of Fe_3O_4NP without altering the crystal lattice pattern. The hydrodynamic size distribution of these two nanoparticles (AuAgNPs and Fe_3O_4NPs) was analyzed by DLS to observe

https://doi.org/10.1021/acsomega.4c05937
ACS Omega 2024, 9, 40051−40060

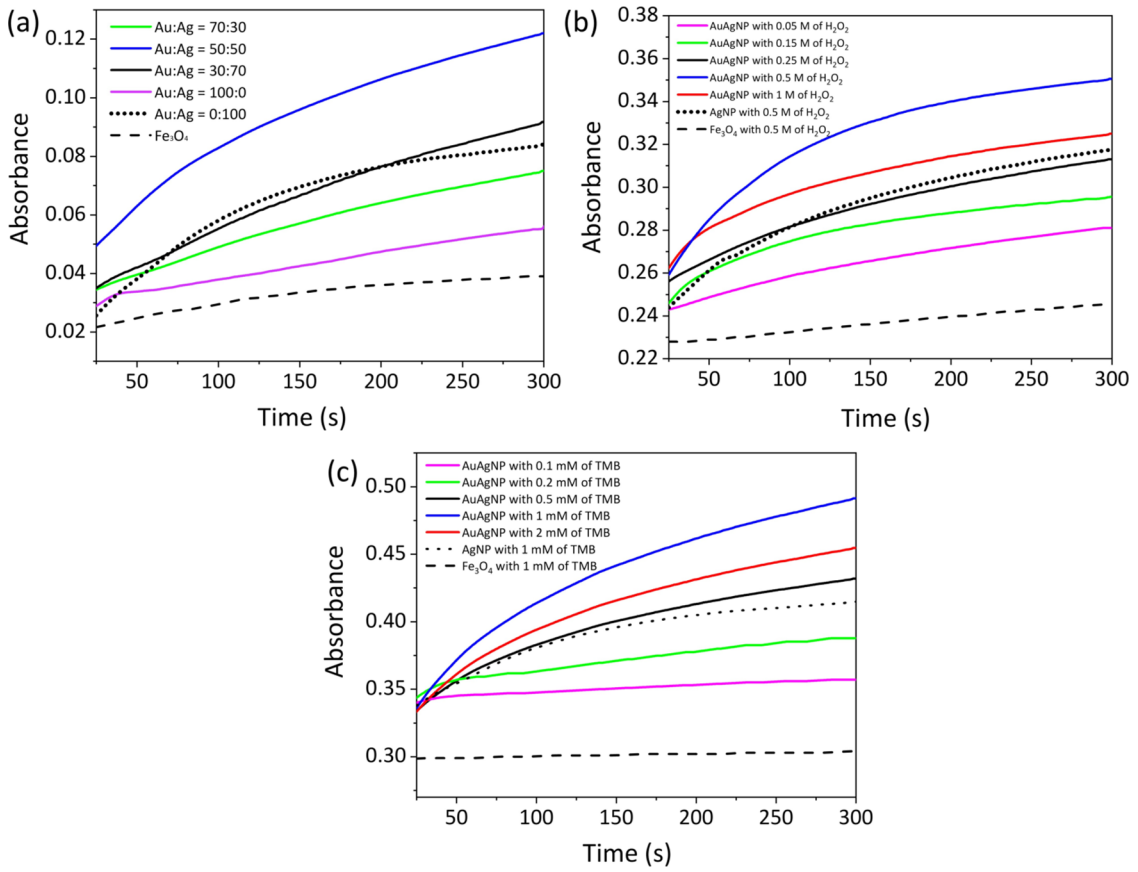

Figure 4. Reaction kinetics of TMB/H_2O_2 with (a) Fe_3O_4NPs and AuAgNPs with various Au and Ag ratios, (b) various H_2O_2 concentrations, and (c) various TMB concentrations.

their properties in solution. As shown in Figure 2(j), the diameters of AuAgNPs, AgNPs, and AuNPs are found to be 70, 20, and 15 nm, respectively. The increase in hydrodynamic sizes from their TEM images can be justified due to their surface charges in the aqueous solution. However, in the case of Fe_3O_4NPs, the sizes are significantly increased, which is attributed to the coagulation effect of the magnetic nanoparticles.

The absorbance spectra (Figure 3(a)) reveal the optical properties of these nanoparticles. As expected, bare Fe_3O_4NPs did not exhibit any absorption. In comparison with bare AgNPs, the absorbance peak of AuAgNPs has shifted significantly from 430[46] to 480 nm, indicating the contribution of AuNPs, whereas bare AuNPs show its peak at 530 nm.[47] The change of color of the solution and the shift of the peak position in absorbance spectra confirm the successful synthesis of bimetallic AuAgNPs. The visual appearance of the AuAgNP also indicates the successful formation of the nanocomposite. Due to the large particle size of AuAgNPs, the dispersion is not stable enough compared to AgNPs and AuNPs. The color of the as-synthesized AuAgNP changes to deep gray in contrast to the typical yellow and pink colors of bare AgNPs and AuNPs, respectively (inset of Figure 3(a)). The dispersion and color change of the solutions indicate the distinct characteristics of AuAgNPs from their individual counterparts.

Noble metal nanoparticles possess peroxidase-like properties, capable of oxidizing TMB in the presence of H_2O_2 to form a blue charge-transfer complex with a maximum absorbance at 655 nm.[48] The catalytic properties of different nanoparticles in the present work were also investigated toward the oxidation of TMB in the presence of H_2O_2, as depicted in Figure 3(b).The self-dissociation of H_2O_2 into radical OH formation is catalyzed by the surface of the AuNP or AgNP. TMB solution in the presence of only H_2O_2 is nearly colorless and becomes blue upon the addition of nanoparticles. TMB coloration by bare AuNPs and AgNPs aligns with the expected results from the literature where the AgNP exhibits higher intensity compared to the AuNP. Notably, the AuAgNPs outperform bare AgNPs within 3 min of interaction, supported by recent findings by Indra et al.[29] The visual color of oxidized TMB is also shown in Figure 3(c). Among the different ratios of Au and Ag precursors tested for synthesis, 80:20 ratio exhibits the highest intensity and fastest reaction rate for TMB oxidation and, thus, was selected for further analysis. On the other hand, the effect of Fe_3O_4NPs on TMB oxidation yields interesting results. The impact of Fe_3O_4NPs on TMB oxidation is initially negligible within the first 3 min. However, over longer intervals of 10 min, the Fe_3O_4NP exhibited gradual intrinsic peroxidase-like activity to mediate TMB oxidation, although at much slower kinetics than AuAgNP. For AuAgNPs, the distinct emergence of the blue color occurs within 3 min, accompanied by a substantial increase in absorbance spectral intensity (Figure S1). Although the catalytic activity of bare Fe_3O_4NPs shows a relatively slow rate initially, its impact on the AuAgNP mixture becomes noticeable over time. The mixture of Fe_3O_4NPs and AuAgNPs demonstrated the highest activity for TMB oxidation. It might be the result of the close association of the Fe_3O_4NPs and AuAgNPs; there is a synergistic effect on the catalytic behavior of AuAgNPs.

https://doi.org/10.1021/acsomega.4c05937
ACS Omega 2024, 9, 40051−40060

Later, this synergistic effect will be confirmed from experimental as well as computational studies.

Optimization of the Sensor. Antibodies were conjugated on both Fe_3O_4NPs and AuAgNPs using EDC/NHS chemistry to achieve a stable attachment. The APTES coating on the Fe_3O_4NP produced amine groups, whereas the AuAgNP, synthesized through citrate reduction, created carboxylic groups. These functional groups were used for antibody conjugation to synthesize AuAgNP and Fe_3O_4NP sensing probes. The rate of TMB oxidation is dependent on physical conditions, such as pH and temperature. Therefore, the reaction conditions were maintained at a standard room temperature of 25 °C and a buffer of pH 4.0 throughout the experiments, which is commonly used in TMB oxidation.[49] The oxidation kinetics of TMB in the presence of H_2O_2 and different concentrations of AuAgNPs were observed by using absorbance spectroscopy. The absorbance of oxidized TMB was directly proportional to the particle concentration (from 1 to 20 μg/mL) in the reaction solution (Figure 4(a)). However, at concentrations exceeding 10 μg/mL, the reaction rate slows compared to the lower concentration range. Therefore, a concentration of 10 μg/mL AuAgNPs was selected for further analysis. Similar optimizations were carried out for TMB and H_2O_2 concentration, separately. Typical Michaelis−Menten curves were obtained by plotting the initial rate of reaction against the concentrations for both H_2O_2 (Figure 4(b)) and TMB (Figure 4(c)). The reaction rate shows a gradual increase from low concentrations of H_2O_2 and TMB and reaches the maximum value at 1 mM for TMB and 0.5 M for H_2O_2, respectively. Therefore, these results indicate that in a particular reaction condition, 10 μg/mL AuAgNPs can trigger the highest signal for the TMB oxidation reaction, where the reactants should have a concentration of 1 mM TMB and 0.5 M H_2O_2. The concentration of Fe_3O_4NP was maintained at 2.5 mg/mL for all experiments to observe the visual effect after separation.

Building upon these experimental findings, this study further investigated the oxidation of TMB in the presence of both AuAgNPs and Fe_3O_4NPs, with the results supported by a theoretical analysis. To explore the interactions and potential synergistic effects, energy-minimized structures of AuAgNPs and the AuAg-Fe_3O_4NP composite were constructed and analyzed, as depicted in Figure 5. Quantum mechanical modeling was performed on TMB and an arbitrarily selected nanocluster, Au_2Ag_6NP (Figure 5(a)). The Au_2Ag_6NP cluster exhibited a somewhat distorted morphology, with frontier MOs dispersed throughout the structure. It is important to note that this cluster was chosen arbitrarily and does not necessarily represent the exact nanocluster morphology observed in TEM images. The Au_2Ag_6NP cluster was then combined with a preformed Fe_3O_4NP single crystal, and the combined structure was optimized by using a mixed basis set to understand the interaction and electronic charge distribution between the components. The resulting elongated structure featured a narrower Fe_3O_4NP end with a dihedral angle of approximately 120°. This configuration suggests that the tricomponent nanoparticles can be effectively accommodated within the TMB structure, as the Fe_3O_4NP (Figure 5(b)) end aligns well with the structural angle of TMB (Figure S5). The energy gap, or HOMO−LUMO gap (HLG), between the HOMO and LUMO provides insights into the ease with which electron densities can be modified, a key factor in understanding potential synergistic effects.[50] The HOMO

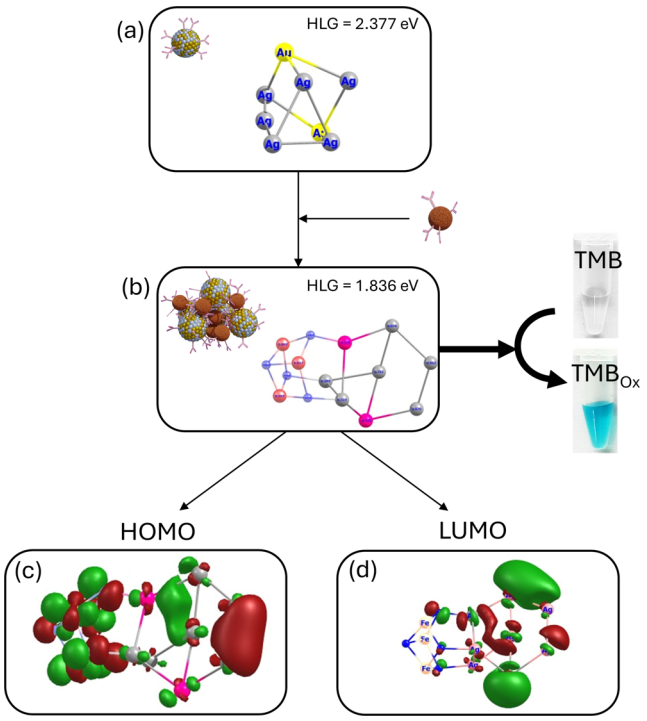

Figure 5. Optimized structures of (a) Au_2Ag_6NP (yellow: Au, gray: Ag) and (b) AuAg-Fe_3O_4NPs (pink: Fe, blue: O, magenta: Au, gray: Ag) and (c) HOMO and (d) LUMO of the nanocomposite.

and LUMO of the AuAg-Fe_3O_4NP composite were simulated (Figure 5(c,d)). The MO mapping indicated that atomic orbitals from both nanoparticles contribute to the linear combination of atomic orbitals, suggesting the formation of an integrated hybrid rather than a simple mixture. Notably, the HOMO of the tricomponent assembly was primarily localized on the Fe_3O_4 portion, while the LUMO was positioned on the AuAg segment of the composite particle. Additionally, the band gap of the Au_2Ag_6NP cluster (initially 1.83 eV) was significantly reduced to 2.38 eV upon combination with Fe_3O_4NP. This reduction supports the likelihood of electron transfer and the resulting synergistic effect between the nanoparticle components.

Sensitivity and Selectivity of Detection. In the absence of DENV-LP, AuAgNPs/Fe_3O_4NPs demonstrate a synergistic enzymatic reaction for TMB oxidation. The change in color intensity is modulated by the attachment of an increasing concentration of the target DENV-LP via sandwich formation. Both nanoparticles have been attached with dengue antibodies to bind with the target DENV-LP. The antibody conjugation of the nanoparticles has been confirmed by standard ELISA procedures with HRP-tagged secondary antibodies. As shown in Figure S4, the antibody-conjugated AuAgNPs and Fe_3O_4NPs show an intense peak at ELISA compared to bare nanoparticles, confirming the attachment of the antibodies. To assess the sensitivity of the proposed method, DENV-LP concentrations ranging from 10 fg/mL to 100 pg/mL were investigated. In Figure 6(a), the absorbance spectra of oxidized TMB with their visual color illustrate distinct changes with various DENV-LP concentrations. In Figure 6(b), a noticeable shift in color, from dark yellow to pale yellow, accompanies the increasing DENV-LP concentration, supported by a decreasing absorption peak at 450 nm. The calibration line in Figure 6(c) reveals a linear range from 10 fg/mL to 100 pg/mL with a

https://doi.org/10.1021/acsomega.4c05937
ACS Omega 2024, 9, 40051−40060

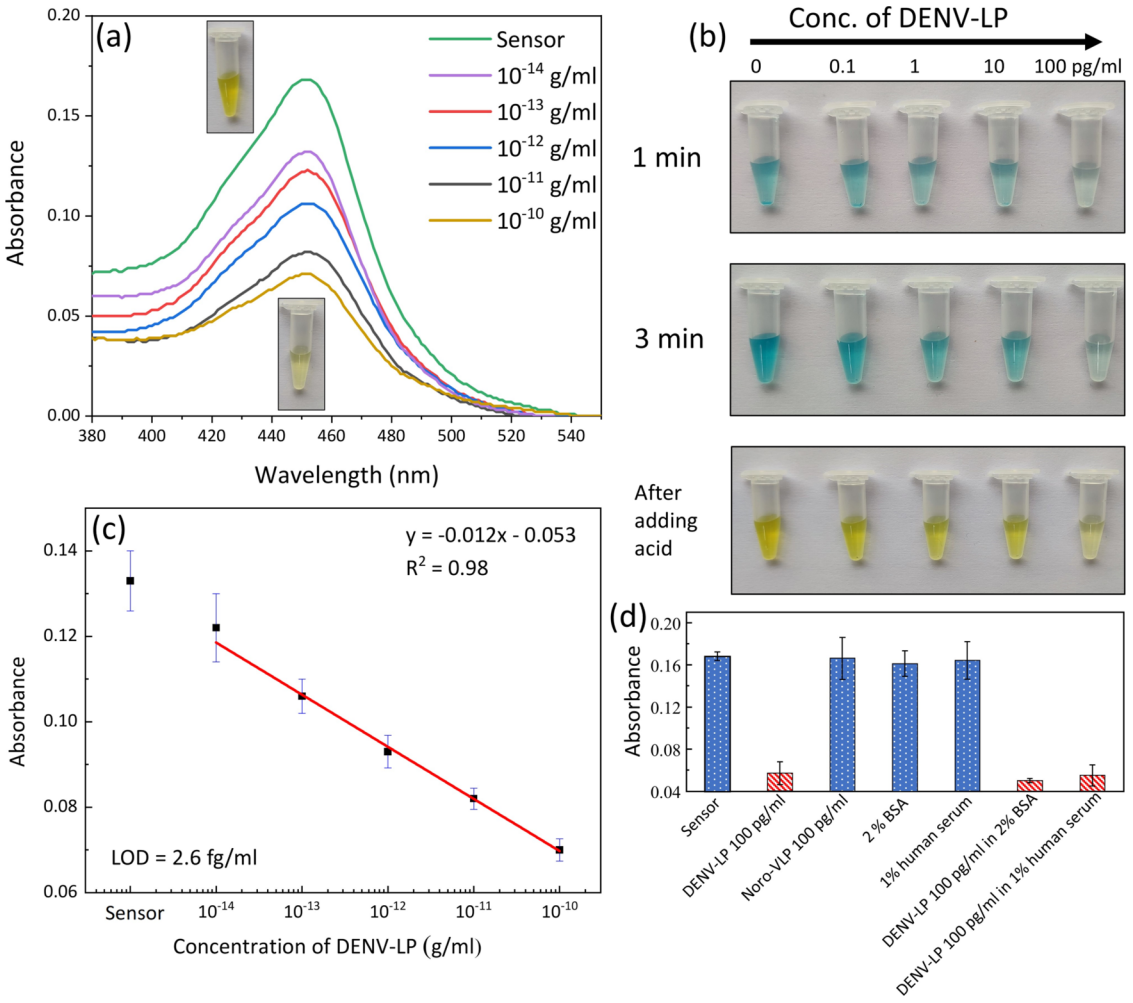

Figure 6. Detection of DENV-LP: (a) absorbance spectra of the AuAgNPs/Fe_3O_4NPs with TMB/H_2O_2 in the presence different concentrations of the DENV-LP, (b) visual coloration of TMB/H_2O_2 before and after acid addition as stop solution, (c) calibration lines from the absorbance spectra, and (d) selectivity of the sensor with other possible interferences.

correlation coefficient of 0.991. The limit of detection (LOD) was determined to be as low as 2.6 fg/mL using the $3\sigma/m$ method, where the σ represents the standard deviation of the lowest signal and m is the slope of the calibration line.[30] The visual color change was distinguishable up to a sample concentration of 100 fg/mL.

The selectivity of this sensing system was assessed with other biological substances such as Noro virus-like particles (NoroV-LP), human serum, and BSA. As shown in Figure 6(d), only the sample containing the DENV-LP exhibits a sharp change in the yellow color of TMB, while the others remain like the bare sensor solutions. Importantly, the sensor successfully recognizes the DENV-LP even when mixed with a 2% BSA and 1% human serum solution, demonstrating the selective nature of the sensor.

This work shows superior sensitivity compared to other recently published studies due to the unique synergistic effect between the AuAgNP and Fe_3O_4NP components, as mentioned in Table 1. This enhancement in sensitivity is evident in the detection of DENV-LP, where the limit of detection (LOD) of 2.6 fg/mL within a linear range of 10 fg/mL−100 pg/mL has been achieved. This outperforms the detection limits reported for other pathogens and viruses in recent studies, such as T7 bacteriophage (18 pM),[47] influenza virus A (H1N1) (44.2 fg/mL),[23] influenza virus A (H3N2) (7.8 HAU),[48] and *Escherichia coli* (10 CFU/mL).[49] Compared with the other analytes, the DENV-LP is relatively small in size and difficult to detect in the low concentration range. However, the synergistic integration of the AuAgNPs with the Fe_3O_4NPs in this system not only enhances the sensitivity but also ensures a robust and reliable detection mechanism.

Table 1. Comparison of This Method with Reported Methods for Detection of Virus/Pathogens Using Colorimetry

virus/pathogens	linear range	LOD	ref
T7 bacteriophage	1.08×10^{10}–4.8×10^{10} PFU/mL	18 pM	51
influenza virus A (H1N1)	5.0×10^{-15}–5.0×10^{-6} g/mL	44.2×10^{-15} g/mL	24
influenza virus A (H3N2)	10–80 HAU	7.8 HAU	52
E. coli	10–10^5 CFU/mL	10 CFU/mL	53
influenza A and B viruses	0.04–40 ng/mL	0.04 ng/mL	54
influenza A virus (H3N2)	$(10–50) \times 10^3$ PFU/mL	3.4 PFU/mL	55
dengue virus-like particles (DENV-LP)	10 fg/mL–100 pg/mL	2.6 fg/mL	this work

https://doi.org/10.1021/acsomega.4c05937
ACS Omega 2024, 9, 40051−40060

The stability of the biosensor demonstrates a notable performance lifespan, maintaining high functionality for up to 21 days before gradually degrading its performance as shown in Figure 7. This stability is attributed to the inorganic nature of

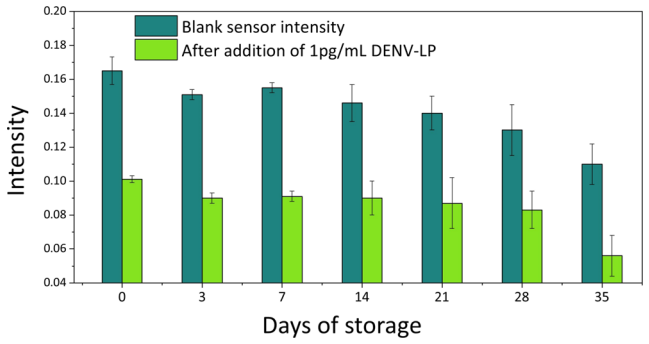

Figure 7. Stability of the sensor over 35 days of preparation.

the AuAgNPs and iron oxide nanoparticles, which are inherently stable. However, the conjugated antibodies on these nanoparticles are sensitive to external environmental factors. When stored at 4 °C under optimal conditions, it is clear from Figure 7 that the sensor retains robust performance throughout the initial 21 days. This period of stability ensures reliable and consistent results for a substantial duration postpreparation, making the biosensor a practical tool for timely and accurate diagnostics before any significant decline in performance begins.

CONCLUSIONS

This work shows an immunoassay that integrates two antibody-coated nanoparticles to significantly improve the sensitivity and specificity of the DENV-LP detection. The Fe_3O_4NPs play a different role in the sensing method other than conventional magnetic separation. It exhibits a strong synergistic effect with the AuAgNPs in TMB coloration, which enhances the sensitivity of the sensor. To the best of our knowledge, this is the first work where the catalytic properties of the Fe_3O_4NPs have been explored for the colorimetric TMB oxidation immunoassay. To understand the mode of combination and electronic charge distribution, the electron transfer and concomitant synergistic effect have been established by the MO distribution of these conjugated nanoparticles. By optimizing the reaction parameters like different nanoparticles, TMB, and H_2O_2 concentrations, the limit of detection could be pushed down to the femtomolar level of 2.6 fg/mL. Control experiments involving nonspecific agents like NoV-LP, BSA, and human serum illustrate the specificity of the sensor for detecting DENV-LP. In summary, through the synergistic integration with Fe_3O_4NPs- and AuAgNPs-catalyzed signal enhancement, this immunoassay provides elevated sensitivity and specificity for detecting the DENV-LP down to femtomolar levels.

ASSOCIATED CONTENT

Supporting Information

The Supporting Information is available free of charge at https://pubs.acs.org/doi/10.1021/acsomega.4c05937.

Reaction kinetics of different nanoparticles with TMB/H_2O_2 over time; ζ-potential and FTIR spectra of the Fe_3O_4NP before and after APTES coating; and optimized structure of TMB (PDF)

AUTHOR INFORMATION

Corresponding Author

Ankan Dutta Chowdhury − *Amity Institute of Nanotechnology, Amity University Kolkata, Kolkata 700135 West Bengal, India;* orcid.org/0000-0002-6391-5895; Email: adchowdhury@kol.amity.edu

Authors

Uddipan Dasgupta − *Amity Institute of Nanotechnology, Amity University Kolkata, Kolkata 700135 West Bengal, India*

Malabika Ghosh − *Amity Institute of Nanotechnology, Amity University Kolkata, Kolkata 700135 West Bengal, India*

Rupali Gangopadhyay − *Department of Chemistry, Sister Nivedita University, Kolkata 700156 West Bengal, India*

Nguyen Thi Ngoc Anh − *Institute of Analytical and Environmental Sciences, National Tsing Hua University, Hsinchu 30013, Taiwan, ROC; Vinh Long University of Technology Education, Vinh Long City 85110, Vietnam*

Ruey-An Doong − *Institute of Analytical and Environmental Sciences, National Tsing Hua University, Hsinchu 30013, Taiwan, ROC;* orcid.org/0000-0002-4913-0602

Provash Chandra Sadhukhan − *Division of Virus Laboratory, ICMR-National Institute of Cholera and Enteric Diseases (NICED), Kolkata 700010, India;* orcid.org/0000-0002-7014-0530

Complete contact information is available at: https://pubs.acs.org/10.1021/acsomega.4c05937

Author Contributions

The manuscript was written through the contributions of all authors. All authors have given approval to the final version of the manuscript. Conceptualization: U.D. and A.D.C.; methodology, validation, and analysis: U.D., M.G., T.N.A., and P.C.S.; characterizations and analysis: U.D. and T.N.A.; writing—original draft preparation: U.D. and A.D.C.; computational modeling and analysis: R.G.; writing—review and editing: R.G., P.C.S., and R.A.D.; supervision: A.D.C.; and project administration: A.D.C. All authors have read and agreed to the published version of the manuscript.

Notes

The authors declare no competing financial interest.

ACKNOWLEDGMENTS

A.D.C. sincerely thanks the Department of Biotechnology for providing Ramalingaswami fellowship (Grant No. BT/RLF/Re-entry/67/2020). We are thankful to Enoch Y. Park, Research Institute of Green Science and Technology, Shizuoka University, Japan, for providing dengue virus-like particles. R Gangopadhyay acknowledges IACS, Kolkata, for providing computational facilities.

REFERENCES

(1) Cassedy, A.; Parle-McDermott, A.; O'Kennedy, R. Virus detection: a review of the current and emerging molecular and immunological methods. *Front. Mol. Biosci.* **2021**, *8*, No. 637559.

(2) Katsarou, K.; Bardani, E.; Kallemi, P.; Kalantidis, K. Viral detection: past, present, and future. *BioEssays* **2019**, *41* (10), No. 1900049.

(3) Burbelo, P. D.; Iadarola, M. J.; Chaturvedi, A. Emerging technologies for the detection of viral infections. *Future Virol.* **2019**, *14* (1), 39−49.
(4) Baker, R. E.; Mahmud, A. S.; Miller, I. F.; Rajeev, M.; Rasambainarivo, F.; Rice, B. L.; Takahashi, S.; Tatem, A. J.; Wagner, C. E.; Wang, L.-F.; et al. Infectious disease in an era of global change. *Nat. Rev. Microbiol.* **2022**, *20* (4), 193−205.
(5) Madhav, N.; Oppenheim, B.; Gallivan, M.; Mulembakani, P.; Rubin, E.; Wolfe, N. Pandemics: Risks, Impacts, and Mitigation. 2018.
(6) Desai, A. N.; Kraemer, M. U.; Bhatia, S.; Cori, A.; Nouvellet, P.; Herringer, M.; Cohn, E. L.; Carrion, M.; Brownstein, J. S.; Madoff, L. C.; Lassmann, B. Real-time epidemic forecasting: challenges and opportunities. *Health Secur.* **2019**, *17* (4), 268−275.
(7) Bhalla, N.; Pan, Y.; Yang, Z.; Payam, A. F. Opportunities and challenges for biosensors and nanoscale analytical tools for pandemics: COVID-19. *ACS Nano* **2020**, *14* (7), 7783−7807.
(8) Park, E. Y.; Takemura, K.; Chowdhury, A. D. Electrode for Electrochemical Measurement. US11,519,876.2022.
(9) Rezvani Jalal, N.; Mehrbod, P.; Shojaei, S.; Labouta, H. I.; Mokarram, P.; Afkhami, A.; Madrakian, T.; Los, M. J.; Schaafsma, D.; Giersig, M.; et al. Magnetic nanomaterials in microfluidic sensors for virus detection: A review. *ACS Appl. Nano Mater.* **2021**, *4* (5), 4307−4328.
(10) Shand, H.; Dutta, S.; Rajakumar, S.; James Paulraj, S.; Mandal, A. K.; KT, R. D.; Ghorai, S. New age detection of viruses: The nano-biosensors. *Front. Nanotechnol.* **2022**, *3*, No. 814550.
(11) Asif, M.; Xu, Y.; Xiao, F.; Sun, Y. Diagnosis of COVID-19, vitality of emerging technologies and preventive measures. *Chem. Eng. J.* **2021**, *423*, No. 130189.
(12) Souf, S. Recent advances in diagnostic testing for viral infections. *Biosci. Horizons: Int. J. Student Res.* **2016**, *9*, hzw010.
(13) Nasrin, F.; Khoris, I. M.; Chowdhury, A. D.; Muttaqein, S. E.; Park, E. Y. Development of disposable electrode for the detection of mosquito-borne viruses. *Biotechnol. J.* **2023**, *18*, 2300125.
(14) Shah, K.; Maghsoudlou, P. Enzyme-linked immunosorbent assay (ELISA): the basics. *Br. J. Hosp. Med.* **2016**, *77* (7), C98−C101.
(15) Boonham, N.; Kreuze, J.; Winter, S.; van der Vlugt, R.; Bergervoet, J.; Tomlinson, J.; Mumford, R. Methods in virus diagnostics: from ELISA to next generation sequencing. *Virus Res.* **2014**, *186*, 20−31.
(16) Clark, M. F.; Lister, R. M.; Bar-Joseph, M. ELISA Techniques. In *Methods Enzymol*; Elsevier, 1986; pp 742−766.
(17) Xu, J.; Liu, Y.; Li, Y.; Liu, Y.; Huang, K.-J. Smartphone-assisted flexible electrochemical sensor platform by a homology DNA nanomanager tailored for multiple cancer markers field inspection. *Anal. Chem.* **2023**, *95* (35), 13305−13312.
(18) Sink, T. D.; Lochmann, R.; Fecteau, K. Validation, use, and disadvantages of enzyme-linked immunosorbent assay kits for detection of cortisol in channel catfish, largemouth bass, red pacu, and golden shiners. *Fish Physiol. Biochem.* **2008**, *34*, 95−101.
(19) Hosseini, S.; Vázquez-Villegas, P.; Rito-Palomares, M.; Martinez-Chapa, S. O.; Hosseini, S.; Vázquez-Villegas, P.; Rito-Palomares, M.; Martinez-Chapa, S. O.Advantages, Disadvantages and Modifications of Conventional ELISA. In *Enzyme-Linked Immunosorbent Assay (ELISA) from A to Z*, SpringerBriefs in Applied Sciences and Technology2018; pp 67−115.
(20) Das, B.; Franco, J. L.; Logan, N.; Balasubramanian, P.; Kim, M. I.; Cao, C. Nanozymes in point-of-care diagnosis: an emerging futuristic approach for biosensing. *Nano-Micro Lett.* **2021**, *13*, 193.
(21) Tang, D.; Cui, Y.; Chen, G. Nanoparticle-based immunoassays in the biomedical field. *Analyst* **2013**, *138* (4), 981−990.
(22) Gao, Z.; Xu, M.; Hou, L.; Chen, G.; Tang, D. Magnetic bead-based reverse colorimetric immunoassay strategy for sensing biomolecules. *Anal. Chem.* **2013**, *85* (14), 6945−6952.
(23) Gurmessa, S. K.; Tufa, L. T.; Kim, J.; Lee, K.-I.; Kim, Y.-M.; Tran, V. T.; Nguyen, H.-Q.; Shim, T. S.; Kim, J.; Park, T. J.; et al. Colorimetric detection of mycobacterium tuberculosis ESX-1 substrate protein in clinical samples using Au@ Pd nanoparticle-based magnetic enzyme-linked immunosorbent assay. *ACS Appl. Nano Mater.* **2021**, *4* (1), 539−549.
(24) Oh, S.; Kim, J.; Tran, V. T.; Lee, D. K.; Ahmed, S. R.; Hong, J. C.; Lee, J.; Park, E. Y.; Lee, J. Magnetic nanozyme-linked immunosorbent assay for ultrasensitive influenza A virus detection. *ACS Appl. Mater. Interfaces* **2018**, *10* (15), 12534−12543.
(25) Lai, W.; Tang, D.; Zhuang, J.; Chen, G.; Yang, H. Magnetic bead-based enzyme-chromogenic substrate system for ultrasensitive colorimetric immunoassay accompanying cascade reaction for enzymatic formation of squaric acid-iron (III) chelate. *Anal. Chem.* **2014**, *86* (10), 5061−5068.
(26) Xu, J.; Liu, Y.; Huang, K.-J.; Hou, Y.-Y.; Sun, X.; Li, J. Real-time biosensor platform based on novel sandwich graphdiyne for ultrasensitive detection of tumor marker. *Anal. Chem.* **2022**, *94* (49), 16980−16986.
(27) Xianyu, Y.; Chen, Y.; Jiang, X. Horseradish peroxidase-mediated, iodide-catalyzed cascade reaction for plasmonic immunoassays. *Anal. Chem.* **2015**, *87* (21), 10688−10692.
(28) Lu, M.; Fu, X.; Xie, H.; Liu, M.; Wei, P.; Zhang, W.; Xie, Y.; Qi, Y. Colorimetric determination of copper ion based on the silver-coated gold nanobipyramids. *J. Food Compos. Anal.* **2023**, *120*, No. 105363.
(29) Khoris, I. M.; Takemura, K.; Lee, J.; Hara, T.; Abe, F.; Suzuki, T.; Park, E. Y. Enhanced colorimetric detection of norovirus using in-situ growth of Ag shell on Au NPs. *Biosens. Bioelectron.* **2019**, *126*, 425−432.
(30) Chowdhury, A. D.; Sharmin, S.; Nasrin, F.; Yamazaki, M.; Abe, F.; Suzuki, T.; Park, E. Y. Use of target-specific liposome and magnetic nanoparticle conjugation for the amplified detection of norovirus. *ACS Appl. Bio Mater.* **2020**, *3* (6), 3560−3568.
(31) Lai, W.; Wei, Q.; Xu, M.; Zhuang, J.; Tang, D. Enzyme-controlled dissolution of MnO2 nanoflakes with enzyme cascade amplification for colorimetric immunoassay. *Biosens. Bioelectron.* **2017**, *89*, 645−651.
(32) Lai, W.; Wei, Q.; Zhuang, J.; Lu, M.; Tang, D. Fenton reaction-based colorimetric immunoassay for sensitive detection of brevetoxin B. *Biosens. Bioelectron.* **2016**, *80*, 249−256.
(33) Peterson, R. D.; Chen, W.; Cunningham, B. T.; Andrade, J. E. Enhanced sandwich immunoassay using antibody-functionalized magnetic iron-oxide nanoparticles for extraction and detection of soluble transferrin receptor on a photonic crystal biosensor. *Biosens. Bioelectron.* **2015**, *74*, 815−822.
(34) Gao, L.; Zhuang, J.; Nie, L.; Zhang, J.; Zhang, Y.; Gu, N.; Wang, T.; Feng, J.; Yang, D.; Perrett, S.; Yan, X. Intrinsic peroxidase-like activity of ferromagnetic nanoparticles. *Nat. Nanotechnol.* **2007**, *2* (9), 577−583.
(35) Khalafalla, S.; Reimers, G. Preparation of dilution-stable aqueous magnetic fluids. *IEEE Trans. Magn.* **1980**, *16* (2), 178−183.
(36) Seifan, M.; Ebrahiminezhad, A.; Ghasemi, Y.; Samani, A. K.; Berenjian, A. Amine-modified magnetic iron oxide nanoparticle as a promising carrier for application in bio self-healing concrete. *Appl. Microbiol. Biotechnol.* **2018**, *102*, 175−184.
(37) Blommaerts, N.; Vanrompay, H.; Nuti, S.; Lenaerts, S.; Bals, S.; Verbruggen, S. W. Unraveling structural information of Turkevich synthesized plasmonic gold−silver bimetallic nanoparticles. *Small* **2019**, *15* (42), No. 1902791.
(38) Chowdhury, A. D.; Nasrin, F.; Gangopadhyay, R.; Ganganboina, A. B.; Takemura, K.; Kozaki, I.; Honda, H.; Hara, T.; Abe, F.; Park, S.; et al. Controlling distance, size and concentration of nanoconjugates for optimized LSPR based biosensors. *Biosens. Bioelectron.* **2020**, *170*, No. 112657.
(39) Frisch, M. *Gaussian 09*, Revision d. 01; Gaussian. Inc: Wallingford CT, 2009; Vol. *201*.
(40) Chowdhury, A. D.; Takemura, K.; Li, T.-C.; Suzuki, T.; Park, E. Y. Electrical pulse-induced electrochemical biosensor for hepatitis E virus detection. *Nat. Commun.* **2019**, *10* (1), No. 3737.
(41) Chowdhury, A. D.; Ganganboina, A. B.; Park, E. Y.; Doong, R.-a. Impedimetric biosensor for detection of cancer cells employing

https://doi.org/10.1021/acsomega.4c05937
ACS Omega 2024, 9, 40051−40060

carbohydrate targeting ability of Concanavalin A. *Biosens. Bioelectron.* **2018**, *122*, 95−103.
(42) Tang, D.; Yuan, R.; Chai, Y. Ligand-functionalized core/shell Ag@ Au nanoparticles label-free amperometric immun-biosensor. *Biotechnol. Bioeng.* **2006**, *94* (5), 996−1004.
(43) Dutta Chowdhury, A.; Ganganboina, A. B.; Tsai, Y.-c.; Chiu, H.-c.; Doong, R.-a. Multifunctional GQDs-Concanavalin A@ Fe3O4 nanocomposites for cancer cells detection and targeted drug delivery. *Anal. Chim. Acta* **2018**, *1027*, 109−120.
(44) Oliveira-Filho, G.; Atoche-Medrano, J. J.; Aragón, F.; Ochoa, J. M.; Pacheco-Salazar, D.; da Silva, S.; Coaquira, J. Core-shell Au/Fe3O4 nanocomposite synthesized by thermal decomposition method: Structural, optical, and magnetic properties. *Appl. Surf. Sci.* **2021**, *563*, No. 150290.
(45) Bondarenko, L.; Illés, E.; Tombácz, E.; Dzhardimalieva, G.; Golubeva, N.; Tushavina, O.; Adachi, Y.; Kydralieva, K. Fabrication, microstructure and colloidal stability of humic acids loaded Fe3O4/APTES nanosorbents for environmental applications. *Nanomaterials* **2021**, *11* (6), 1418.
(46) Yao, Y.; Cao, S.; Zhang, X.; Yan, J.; Li, W.; Whittaker, A. K.; Zhang, A. Microconfinement from dendronized chitosan oligosaccharides for mild synthesis of silver nanoparticles. *ACS Appl. Nano Mater.* **2022**, *5* (3), 4350−4359.
(47) Khlebtsov, B. N.; Tumskiy, R. S.; Burov, A. M.; Pylaev, T. E.; Khlebtsov, N. G. Quantifying the numbers of gold nanoparticles in the test zone of lateral flow immunoassay strips. *ACS Appl. Nano Mater.* **2019**, *2* (8), 5020−5028.
(48) Cai, S.; Yang, R. Noble metal-based nanozymes. *Nanozymol.: Connect. Biol. Nanotechnol.* **2020**, 331−365.
(49) Xing, L.; Zheng, X.; Tang, Y.; Zhou, X.; Hao, J.; Hu, L.; Shen, J.; Yan, Z. Ag-β-cyclodextrin-graphene oxide ternary nanostructures with peroxidase-mimicking activity for Hg2+ detection. *ACS Appl. Nano Mater.* **2021**, *4* (12), 13807−13817.
(50) Gangopadhyay, R. How does PEDOT grow like nanoropes? A theoretical investigation in pace with experimental insights. *J. Mol. Liq.* **2020**, *316*, No. 113739.
(51) Lesniewski, A.; Los, M.; Jonsson-Niedziółka, M.; Krajewska, A.; Szot, K.; Los, J. M.; Niedziolka-Jonsson, J. Antibody modified gold nanoparticles for fast and selective, colorimetric T7 bacteriophage detection. *Bioconjugate Chem.* **2014**, *25* (4), 644−648.
(52) Liu, Y.; Zhang, L.; Wei, W.; Zhao, H.; Zhou, Z.; Zhang, Y.; Liu, S. Colorimetric detection of influenza A virus using antibody-functionalized gold nanoparticles. *Analyst* **2015**, *140* (12), 3989−3995.
(53) Kwon, D.; Lee, S.; Ahn, M. M.; Kang, I. S.; Park, K.-H.; Jeon, S. Colorimetric detection of pathogenic bacteria using platinum-coated magnetic nanoparticle clusters and magnetophoretic chromatography. *Anal. Chim. Acta* **2015**, *883*, 61−66.
(54) Raji, M. A.; Aloraij, Y.; Alhamlan, F.; Suaifan, G.; Weber, K.; Cialla-May, D.; Popp, J.; Zourob, M. Development of rapid colorimetric assay for the detection of Influenza A and B viruses. *Talanta* **2021**, *221*, No. 121468.
(55) Ahmed, S. R.; Kim, J.; Suzuki, T.; Lee, J.; Park, E. Y. Enhanced catalytic activity of gold nanoparticle-carbon nanotube hybrids for influenza virus detection. *Biosens. Bioelectron.* **2016**, *85*, 503−508.

https://doi.org/10.1021/acsomega.4c05937
ACS Omega 2024, 9, 40051−40060